Benchmarking the Performance of the ReaxFF Reactive Force Field on Hydrogen Combustion Systems

Luke W. Bertels,[†] Lucas B. Newcomb,[‡] Mohammad Alaghemandi,[‡] Jason R. Green,[‡,¶] and Martin Head-Gordon[∗,†,§]

[†]*Department of Chemistry, University of California, Berkeley, California 94720, USA.*
[‡]*Department of Chemistry, University of Massachusetts Boston, Boston, MA 02125, USA.*
[¶]*Department of Physics, University of Massachusetts Boston, Boston, MA 02125, USA.*
[§]*Chemical Sciences Division, Lawrence Berkeley National Laboratory, Berkeley, California 94720, USA.*

E-mail: mhg@cchem.berkeley.edu

Abstract

A thorough understanding of the kinetics and dynamics of combusting mixtures is of considerable interest, especially in regimes beyond the reach of current experimental validation. The ReaxFF reactive force field method has provided a way to simulate large-scale systems of hydrogen combustion via a parameterized potential that can simulate bond breaking. This modeling approach has been applied to hydrogen combustion, as well as myriad other reactive chemical systems. In this work, we benchmark the performance of several common parameterizations of this potential against higher-level quantum mechanical (QM) approaches. We demonstrate instances where these parameterizations of the ReaxFF potential fail both quantitatively and qualitatively to describe reactive events relevant for hydrogen combustion systems.

Introduction

Hydrogen combustion is a promising energy source for both space exploration[1] and cleaner terrestrial transportation.[2–5] Hydrogen is an attractive fuel in part because of its high energy density and lack of carbon-containing combustion products.[6–8] Such applications require understanding of how the chemistry of hydrogen and hydrogen combustion plays a role in storage, efficiency, and safety.[1,4,9–13] Furthermore, many of the elementary reactions relevant to hydrogen combustion are present in the combustion of other hydrogen-containing fuels.[14]

Extensive effort has been made to model the reaction kinetics of hydrogen combustion under a variety of conditions with ample feedback from experimental studies. Mueller et al.[15] developed a model based on their experimental findings to accurately describe the kinetics below the second explosion limit. Li et al.,[16] beginning from the mechanisms proposed by Mueller et al., updated the model by modifying reaction rates to better predict high-pressure flame speed experiments. O'Connaire et. al[17] also developed a new mechanism validated on flames speeds, ignition time delays, and species composition, also modifying reaction rates to better account for higher pressure experiments. Konnov,[18] in updating the H_2/O_2 combustion mechanism, provided better analysis of the uncertainties in reaction rates and suggested the importance of $HO_2 + H$ reactions in accurately predicting ignition delays. Hong et. al.[19] proposed updates to reaction rates based on their UV and IR measurements on high-temperature mixtures in shock tubes. Burke et al.[20] developed a model based on the Li mechanism that can push to more intermediate pressures towards the second extended explosion limit. To better treat high pressures, Shimuzi et al.,[21] building of the work of Kitano et al.,[22] further investigated the importance of $HO_2 + H$ reactions and called for more accurate rate constats to be determined for several reactions. The development of the ELTE mechanism by Varga et. al[23] involved a global optimization of parameters and considered all available direct and indirect measurements for evaluation. The authors also benchmarked the performance of a variety of previous models on their measurement set. An experimental study of laminar flames across a wide parameter range was complemented by

quantum-chemical calculations of rates constants and shock tube data to develop the HP-Mech model and extract pressure-dependent reaction orders[24] Burke and Klippenstein,[25] investigating the elementary reactions of hydrogen combustion via a *ab initio*-master equation, proposed inclusion of new three-body radical propogation and termination reactions. Recent work by Konnov,[26] however, has suggested that new transport parameters suggested by Jasper et al.[27,28] provided a better match to flame speeds than the inculsion of Burke and Klippenstein's new reactions. Experimental studies on the roles of impurities in shock tube data have also been recently performed.[29] Sabia et al.,[30] in an experimental work to better quantify the role that different bath gases, has found existing models lacking for bath gases other than N_2. In this work, the authors also highlight several existing challenges in the modeling of hydrogen combustion, including uncertainties in rate constants, unconsidered or excluded reaction mechanisms, and uncertainties relating to three-body effects. A more complete review of the history, current standings, and challenges of modeling H_2 combustion is given in the discussion of their work.[30]

Three of us[31–36] have recently developed and applied a method of reactive symbol sequences to the study of hydrogen combustion as an alternative route to analyze chemical kinetics. This framework avoids the ideas of elementary reactions and rate coefficients, both of which can be strongly dependent on modeling assumptions.[37,38] Instead, reactive symbol sequences can be seen as a way to probe the emergent chemical processes present in combustion chemistry. Applied to reactive molecular dynamics (MD), this approach naturally includes important non-equilibrium fluctuations. Beginning with an all-atom potential function that depends only on the atomic positions, in principle also allows for a method to be predictive from the outset instead of relying on parameterization which is only relevant near the particular conditions on which it is trained.[39]

To generate the trajectories for this approach, one could, in principle, consider using *ab initio* MD simulations where energies and forces are determined using electronic structure theory methods. Examples of this include the nanoreactor studies in which pressure and

temperature fluctuations are used to induce reactive events.[40,41] Despite their accuracy for barrier heights and reaction energies, the high computational cost of these methods limits both the size and timescale of simulations.

Alternatively, empirical methods including reactive force fields[39,42–47] and tight binding[48–50] offer a computationally more feasible approach to larger and longer simulations, though potentially with a loss of accuracy. The former allow for the nanosecond scale simulations on thousands of atoms. Within the ReaxFF reactive force field,[39] energies are determined via a combination of connection dependent terms based on bond orders and a polarizable charge description. These potentials depend on system-specific parameters which are trained against QM data, including reaction energies and barrier heights. ReaxFF potentials have been developed and applied to combustion reactions,[51–67] including hydrocarbons, hydrogen,[54,63] and syngas.[67] The ReaxFF method has also been extensively applied to material science,[68–83] catalysis,[84–88] and other chemical systems.[39,89–97]

The reactive symbol sequence studies for hydrogen combustion cited above have utilized ReaxFF potentials in order to generate the trajectories required for their analysis. While ReaxFF potential are derived from fits to QM data, there are no reports available on assessment of ReaxFF parameterizations against independent test sets of QM data at combustion relevant atomic configurations. In this work, we benchmark the performance of several ReaxFF parameter sets on a set of trajectories and reactions relevant to the combustion of hydrogen. The predictive power of the ReaxFF method hinges on its fidelity to QM data, especially in conditions where experimental validation is difficult or impossible.

Computational Methods

ReaxFF Reactive Force Field Method

ReaxFF is an atomistic potential capable of describing reactive events. Bond breaking and formation are captured in ReaxFF via computed bond orders between pairs of atoms.

Intramolecular bonded energy contributions are captured using potential functions that depend on these bond orders, which are determined by the interatomic distances. Nonbonded intermolecular interactions including Coulomb, dispersion, and polarization are computed between all pairs of atoms using geometry-dependent charge equilibration schemes and are damped at short range.[98,99] Analytic forms for these potential functions can be found in the the supporting information of Chenoweth et al.[51] The total potential is:

$$
\begin{aligned}
E_{\text{system}} =& E_{\text{bond}} + E_{\text{lp}} + E_{\text{over}} + E_{\text{under}} + E_{\text{val}} + E_{\text{tor}} \\
& + E_{\text{coa}} + E_{\text{conj}} + E_{\text{H-bond}} + E_{\text{vdW}} + E_{\text{coul}} + E_{\text{pol}}
\end{aligned}
\tag{1}
$$

where E_{bond}, E_{lp}, E_{over}, E_{under}, E_{val}, E_{tor}, E_{coa}, E_{conj}, $E_{\text{H-bond}}$, E_{vdW}, E_{coul}, and E_{pol}, are the bond, lone pair, overcoordination, undercoordination, valence angle, torsional angle, three-body conjugation, four-body conjugation, hydrogen bond, van der Waals, Coulomb, and polarization energy contributions, respectively.

For a given class of chemical systems, parameters for these energy contributions were trained on a data set comprised of electronic structure theory calculations and experimental data. For the purposes of this work, we have selected four combustion-specific parameter sets of the ReaxFF force field to benchmark against high-level QM calculations.

1. The CHO2008 parameter set was developed in 2008 by Chenoweth, van Duin, and Goddard was a first parameterization of a ReaxFF potential for hydrocarbon oxidation.[51]

2. The HO2011 parameter set was developed in 2011 by Agrawalla and van Duin specifically to simulate hydrogen combustion at high temperature and pressure.[54]

3. The HO2014 parameter set was developed in 2014 by Cheng et al. as a reoptimization of the CHO2008 set for use in accelerated reactive molecular dynamics simulations.[63]

4. The CHO2016 parameter set was developed in 2016 by Ashraf and van Duin as a systematic improvement of the CHO2008 to better capture small hydrocarbon oxidation

and combustion initiation.[67]

Our single-point calculations were performed using the reax/c package[100] as implemented in LAMMPS (`http://lammps.sandia.gov`).[101]

Molecular Dynamics Simulations

Molecular dynamics trajectories were calculated using the HO2011 parameter set[54] with the ReaxFF potential.[51] All trajectories simulations were carried out with constant particle number, volume, and energy (NVE) and utilized a time step of 0.1 fs and periodic boundary conditions.

We first considered a high-pressure simulations initialized with 66 H_2 molecules, 33 O_2 molecules, and an OH radical initiator at an initial pressure of 950 bar and an initial temperature of 1000 K (initial density $\rho_0 = 250$ kg m^{-3}, stoicheometric ratio $\phi = 1$). These trajectories were allowed to evolve for 3 ns, at which point more than 80% of the reactants were converted to water.[32] This set of trajectories was calculated using the PuReMD-GPU simulation package.[102] This set of trajectories has already been reported and analyzed using reactive symbol sequences.[32]

A larger, lower pressure simulation was also performed to better isolate bimolecular reactive events. This simulation was initialized with 320 H_2 molecules, 160 O_2 molecules, and 16 OH radical initiators at an initial pressure of 50 bar and an initial temperature of 1250 K ($\rho_0 = 5.9$ kg m^{-3}, $\phi = 1$). This trajectory was allowed to evolve for approximately 70 ns, at which point the temperature had equilibrated and the reactants were nearly completely converted to water. The OH radicals were added to initiate the ignition of the reaction mixture. Figure 1 presents the kinetic temperature of this reacting mixture as a function of simulation time. This trajectory was calculated using the reax/c package[100] in LAMMPS.[101]

From the simulated MD trajectories under these high and low pressure conditions, "reactive pathways" were extracted during the ignition events that characterize the combustion reaction at fixed energy.[32] These paths correspond to isolated elementary bi- and ter-
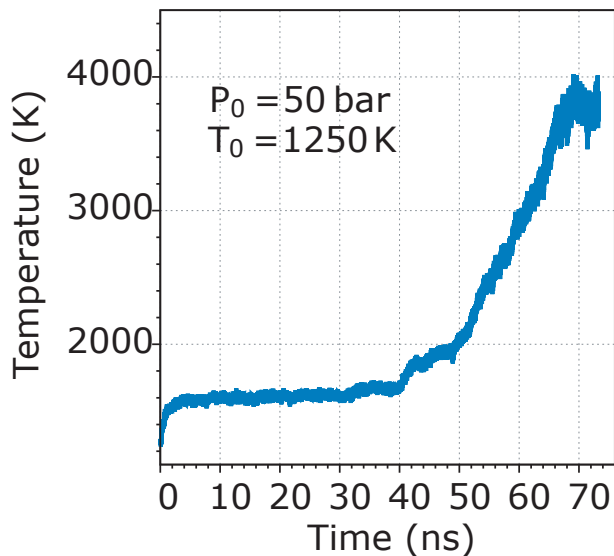
Figure 1: Time series of the kinetic temperature for a hydrogen-oxygen mixture that is initially stoichiometric at a temperature of 1250 K and pressure of 50 bar.

molecular reaction events. Because they occur naturally during the course of ignition, the paths of these reactions through the transition state regions include oscillations about the spectator modes. These reactive paths are a point of comparison to minimum energy paths found via quantum-mechanical calculations.

Quantum-Mechanical Calculations

In order to benchmark the performance of the ReaxFF potential, QM calculations were performed using coupled cluster theory with single, double, and perturbative triple excitations [CCSD(T)][103] in the spin-unrestricted wave function formalism utilizing the frozen-core approximation and the cc-pVTZ basis set[104] and extrapolated to the complete basis set limit. The correlation energy was extrapolated with second-order Møller-Plesset perturbation theory using the resolution of the identity approximation (RI-MP2).[105,106] The expression for

this overall extrapolated energy is

$$E(\text{CCSD(T)/CBS}) = E(\text{HF/cc-pV5Z}) + E^{\text{corr}}(\text{RI-MP2/CBS}_{3,4,5}) +$$
$$E^{\text{corr}}(\text{CCSD(T)/cc-pVTZ}) - E^{\text{corr}}(\text{RI-MP2/cc-pVTZ}) \tag{2}$$

where $E^{\text{corr}}(\text{RI-MP2/CBS}_{3,4,5})$ is the extrapolated RI-MP2 correlation energy using the cc-pVTZ, cc-pVQZ, and cc-pV5Z basis sets[104] to fit

$$E^{\text{corr}}(\text{RI-MP2/cc-pVNZ}) = E^{\text{corr}}(\text{RI-MP2/CBS}_{3,4,5}) + AN^{-3} \tag{3}$$

and N is the cardinality of the cc-pVNZ basis set.[107] From comparisons between extrapolated CCSD(T) and composite Weizmann methods as well as evaluation of CCSD(T) for bond stretching, we predict errors in our benchmark calculations on the order of 1–4 kcal mol^{-1}.[108–110]

As another point of comparison, QM calculations were also performed using the ωB97M-V[111] density functional in the spin-unrestricted wave function formalism with the cc-pVTZ basis set.[104] This functional has been ranked as one of the most accurate in a recent assessment of 200 density functionals on systems including thermochemistry and barrier heights.[112] All DFT calculations were carried out using an ultra-fine integration grid using 99 radial points and 590 angular points.

In addition to the reactive pathways harvested from MD simulations, intrinsic reaction coordinate scans for a subset of bimolecular reactions relevant to hydrogen combustion from Li et al.[16] were used for benchmarking systems. Structures for the products and reactants were computed via geometry optimization at the ωB97M-V/cc-pVTZ level of theory. Transition structures were computed using the freezing string method[113] to generate an approximate structure and Hessian, then refined by the partitioned-rational function optimization eigenvector following method (P-RFO),[114] also at the ωB97M-V/cc-pVTZ level of theory. Vibrational analysis was used to confirm that the minima have no imaginary frequencies and

that the transition state structures have only one imaginary frequency. The reaction path on either side of the transition state structure was computed using the intrinsic reaction coordinate method.[115–117] All QM calculations were performed using the Q-Chem[118] package of electronic structure programs.

Results and discussion

Reactive Pathways

A collection of seven reactive pathways were harvested from larger MD simulations and are presented in order to benchmark the performance of ReaxFF against electronic structure theory calculations. By this, we mean that the coordinates of all spectator species are removed, leaving a relatively small subset of atoms undergoing chemical changes, whose relative energies can be tractably benchmarked. As the overall MD simulations were performed with the HO2011 parameter set, energies of the configurations along these pathways will be relative to energies of the isolated reactants at geometries optimized with ReaxFF using the HO2011 parameter set.

Two termolecular reactions were extracted from the high-pressure simulation ($N_{H_2,0} = 66$, $N_{O_2,0} = 33$, $N_{OH,0} = 1$, $P_0 = 950$ bar, $T_0 = 1000$ K, $\rho_0 = 250$ kg m^{-3}, $\phi = 1$). The first of these reactions is the near simultaneous cleaving of a hydrogen molecule by an oxygen atom and an oxygen molecule to yield a hydroxyl radical and a hydroperoxyl radical (O + H_2 + O_2 $\longrightarrow$ OH + HO_2). For the *ab initio* calculations the ground state is a singlet. The second of these termolecular reactions is the cleaving of a hydrogen molecule by an oxygen molecule and a hydroperoxyl radical to form a hydroperoxyl radical and hydrogen peroxide ($O_2 + H_2 + HO_2$ $\longrightarrow$ $HO_2 + H_2O_2$). The ground state is a doublet for this reaction. Plots of the potential energy along the pathways for the methods surveyed are presented in Figures S1–S2.

In addition to these termolecular reactive pathways, five bimolecular reactive pathways

were extracted from the 50 bar simulation ($N_{H_2,0} = 320$, $N_{O_2,0} = 160$, $N_{OH,0} = 16$, $P_0 = 50$ bar, $T_0 = 1250$ K, $\rho_0 = 5.9$ kg m^{-3}, $\phi = 1$). The first of these is the initiation reaction between a hydrogen molecule and an oxygen molecule forming a hydroperoxyl radical and a hydrogen atom ($H_2 + O_2 \longrightarrow HO_2 + H$), which has a triplet ground state. The second is the reaction of a hydrogen atom and an oxygen molecule to form a hydroperoxyl radical ($H + O_2 \longrightarrow HO_2$), which has a doublet ground state. Third is the the reaction of a hydroperoxyl radical and a hydrogen atom to form two hydroxyl radicals ($HO_2 + H \longrightarrow 2\,OH$), occurring on the singlet surface. Fourth and fifth are both reactions of hydrogen molecules and hydroxyl radicals to form water and a hydrogen atom ($H_2 + OH \longrightarrow H_2O + H$), which have doublet ground states. Plots of the potential energy along the trajectories for the methods surveyed are presented in Figures 2,S3–S7.

Table 1 presents the root mean square deviations (RMSD), mean signed deviation (MSD), maximum absolute deviation (MAX), and non-parallelity error (NPE), all in kcal mol^{-1}, for pathways extracted from MD simulations. Here, the non-parallelity error is defined as the difference between the maximum and minimum error along a reaction pathway. For the overall metrics, the modern density functional, ωB97M-V, unsurprisingly outperforms all of the surveyed ReaxFF methods by a factor of 4 for RMSDs, 2 for MSDs, 7 for MAXs, and 7 for NPEs. Of the ReaxFF methods, the CHO2016 parameter set outperforms the other parameter sets in terms of RMSDs, MSDs, and MAXs with values of 11.44 kcal mol^{-1}, -2.59 kcal mol^{-1}, and 41.07 kcal mol^{-1}, respectively. The next-best performing parameter set for these properties was HO2011, followed by HO2014 and CHO2008, respectively. The CHO2008 parameter set performs the best for NPEs with a value of 53.70 kcal mol^{-1}. The negative MSDs for all methods demonstrates a systematic overstabilization of configurations relative to isolated reactants. Furthermore, the NPEs in excess of 15 kcal mol^{-1} and up to 90 kcal mol^{-1} demonstrate that ReaxFF does not capture the shape of the potential energy surfaces along the reactive pathways.

As an example, Figure 2 presents the potential energy along the first $H_2 + OH \longrightarrow$

Table 1: Root mean square deviation, mean signed deviation, maximum absolute deviation, and non-parallelity error, in kcal mol^{-1}, are presented for a selection of reactive pathways extracted from larger MD simulations. CCSD(T)/CBS values were used as reference.

Reaction	Method	RMSD	MSD	MAX	NPE
$O + H_2 + O_2 \longrightarrow OH + HO_2$	ωB97M-V	3.00	-2.51	-4.81	5.28
	CHO2008	59.54	-57.06	-77.33	53.70
	HO2011	41.55	-38.49	-58.41	57.93
	HO2014	28.18	-26.18	-45.20	32.14
	CHO2016	18.93	-10.78	-41.07	55.93
$O_2 + H_2 + HO_2 \longrightarrow HO_2 + H_2O_2$	ωB97M-V	2.02	0.74	4.38	7.33
	CHO2008	35.49	-33.70	-61.14	43.02
	HO2011	28.98	-24.46	-55.46	62.44
	HO2014	32.58	-29.67	-55.45	60.57
	CHO2016	16.86	-6.94	-37.15	58.38
$H_2 + O_2 \longrightarrow HO_2 + H$	ωB97M-V	1.21	-0.43	-2.77	3.91
	CHO2008	22.34	-19.36	-37.54	32.87
	HO2011	16.35	-13.51	-32.23	35.36
	HO2014	11.31	3.30	17.02	30.45
	CHO2016	8.40	-0.94	-18.31	34.08
$H + O_2 \longrightarrow HO_2$	ωB97M-V	2.17	1.57	4.79	5.10
	CHO2008	11.37	-10.63	-21.88	17.73
	HO2011	10.03	-1.21	15.43	30.85
	HO2014	12.60	-8.27	17.90	34.42
	CHO2016	8.63	-3.92	-14.17	26.69
$HO_2 + H \longrightarrow 2\,OH$	ωB97M-V	4.11	3.68	6.00	6.43
	CHO2008	18.06	5.64	26.88	53.42
	HO2011	8.55	2.43	-17.35	33.95
	HO2014	21.08	-4.21	-59.19	90.63
	CHO2016	14.80	-1.80	-38.68	58.01
$H_2 + OH \longrightarrow H_2O + H$	ωB97M-V	1.69	-0.50	-3.42	5.79
	CHO2008	14.66	-10.58	-28.76	33.98
	HO2011	8.29	-3.46	-20.16	32.29
	HO2014	8.27	-4.02	-15.89	24.25
	CHO2016	10.48	-4.62	-19.28	32.09
$H_2 + OH \longrightarrow H_2O + H$	ωB97M-V	1.94	0.03	3.11	5.47
	CHO2008	9.64	-4.75	-20.49	28.76
	HO2011	8.05	-2.24	-16.22	26.00
	HO2014	5.99	-1.60	-11.26	22.42
	CHO2016	8.72	7.61	16.81	28.94
All Pathways	ωB97M-V	2.62	1.07	6.00	7.33
	CHO2008	18.32	-8.30	-77.33	53.70
	HO2011	12.46	-3.56	-58.41	62.44
	HO2014	15.10	-5.25	-59.19	90.63
	CHO2016	11.44	-2.59	-41.07	58.38

H$_2$O+H reactive pathway for the CCSD(T) reference, ωB97M-V, and four ReaxFF parameter sets. Like the others, this reactive pathway was sampled from a larger mixture undergoing ignition. This particular reactive path begins with the rotation of a H$_2$ molecule relative to an OH radical, followed attack by the OH radical and oscillation of the transferring H atom between the OH and H fragments until a H$_2$O molecule and H atom are left. Of the ReaxFF potentials, the HO2014 parameter set yields the best RMSD, MAX, and NPE of 8.27 kcal mol^{-1}, -15.89 kcal mol^{-1}, and 24.25 kcal mol^{-1}, respectively. The HO2011 parameter set yields the best MSD of -3.46 kcal mol^{-1}. Qualitatively, the positions of local minima and maxima for the HO2014 and CHO2016 parameter sets agree with the reference calculations, though the actual values at these extrema often differ by over 10 kcal mol^{-1}. The same can be said for the CHO2008 and HO2011 parameter sets in the first 100 time steps as well, however the CHO2008 parameter set significantly underestimates the barrier for hydrogen transfer. The HO2011 parameter set gives the most jarring performance qualitatively, with sharp features arising in the region of oscillation of H between OH and H.
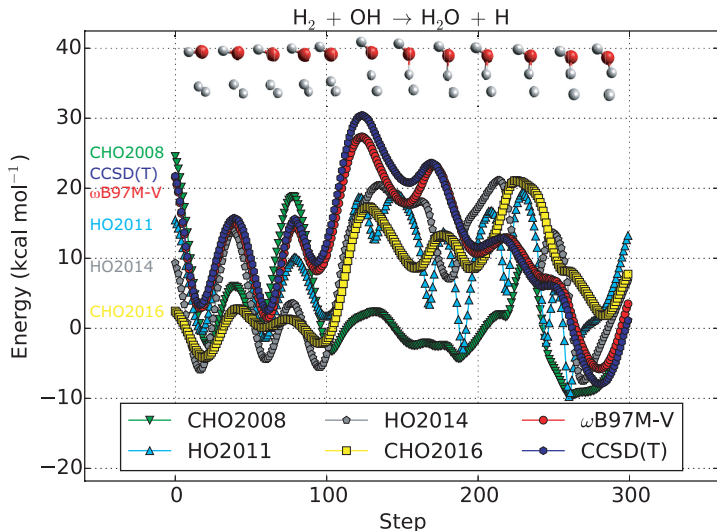

Figure 2: Potential energy along the first H$_2$+OH $\longrightarrow$ H$_2$O+H reactive pathway, extracted from a larger MD simulation. The parent simulation was run using ReaxFF with the HO2011 parameter set. The energies presented are relative to the energies of isolated H$_2$ and OH computed at the ReaxFF/HO2011 optimized geometries.The total time to complete this reaction path is 30 fs with a time step of 0.1 fs.

In order to probe the origin of the sharp features in the HO2011 potential energy surface, we investigated the component-wise contributions to the potential energy. Figure 3 shows the overall potential energy, atom energy, and the difference, all in kcal mol^{-1}. Here the atom energy is defined as the sum of the overcoordination energy E_{over} and undercoordination energy E_{under}. For the HO2011 parameter set, the sharp features in the overall potential energy can be traced to the atom energy, whereas for all other parameter sets this contribution changes much more smoothly. In this term, positive contributions are seen to arise mainly from overcoordination of the transferring hydrogen atom whereas negative contributions arise from undercoordination of the OH radical in the entrance channel and H in the exit channel.

Intrinsic Reaction Coordinate Scans

We have calculated intrinsic reaction coordinate (IRC) scans for a subset of bimolecular reactions taken from Li et al.[16] as an additional set of systems on which to evaluate the performance of ReaxFF. These IRC scans were calculated at the ωB97M-V/cc-pVTZ level of theory. Energies of isolated reactant and product species were also calculated at the ωB97M-V/cc-pVTZ optimized geometries to present relative energies and compute reaction energies and barrier heights. Eleven scans are included (see Table 2 for the full list): the radical attack of a hydrogen atom and an oxygen molecule to form a hydroxyl radical and an oxygen atom ($\text{H} + \text{O}_2 \longrightarrow \text{OH} + \text{O}$) on the quartet surface, the abstraction of hydrogen from a hydrogen molecule by a hydroxyl radical to form a water molecule and a hydrogen atom ($\text{H}_2 + \text{OH} \longrightarrow \text{H}_2\text{O} + \text{H}$) on the doublet surface, the abstraction of hydrogen from a water molecule by an oxygen atom to form two hydroxyl radicals ($\text{H}_2\text{O} + \text{O} \longrightarrow 2\,\text{OH}$) on the triplet surface, the formation of a hydroperoxyl radical from a hydrogen atom and an oxygen molecule ($\text{H} + \text{O}_2 \longrightarrow \text{HO}_2$) on the doublet surface, the abstraction of hydrogen from a hydroperoxyl radical by a hydrogen atom to form a hydrogen molecule and an oxygen molecule ($\text{HO}_2 + \text{H} \longrightarrow \text{H}_2 + \text{O}_2$) on the triplet surface, the radical attack of a hydrogen atom
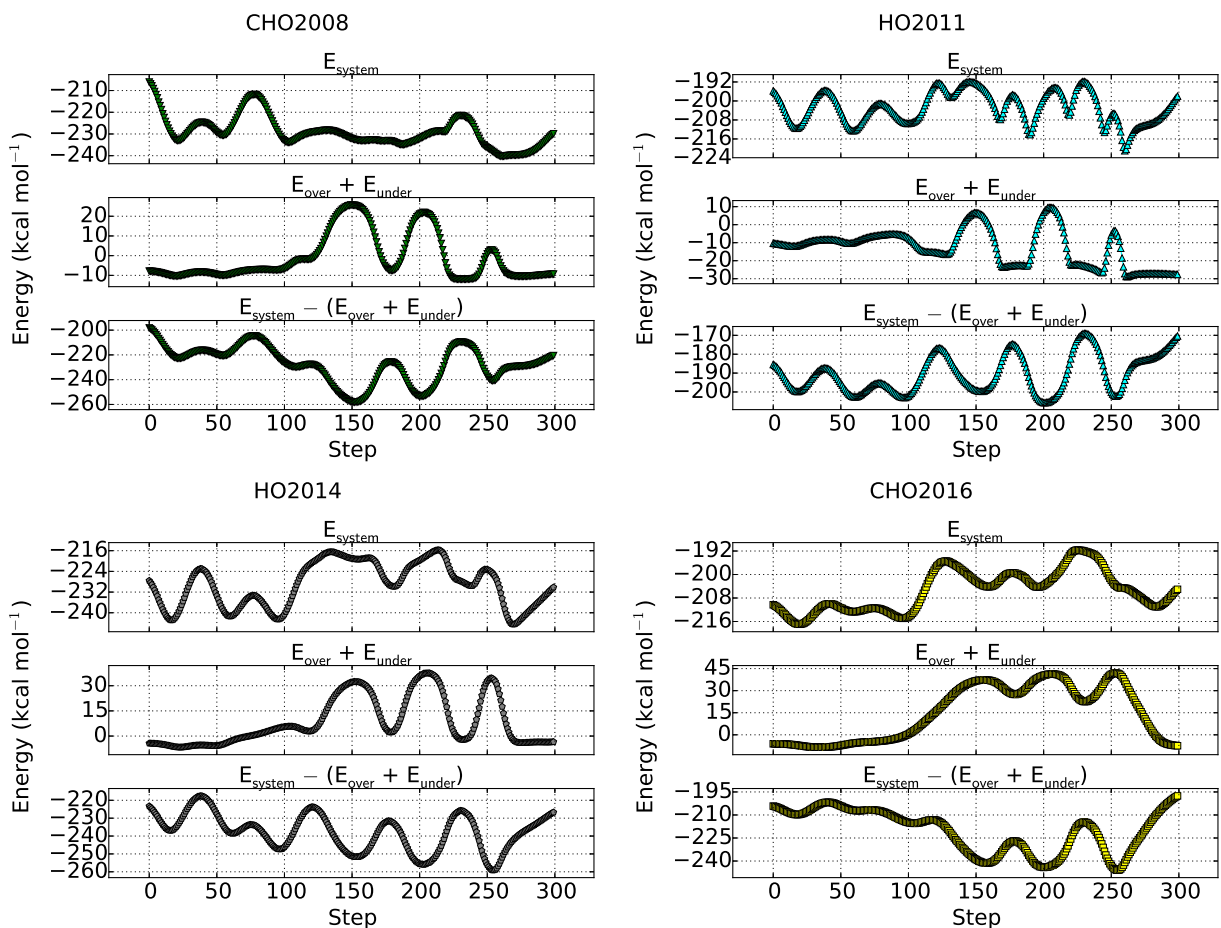
Figure 3: Potential energy, atom energy, and the sum of all other energy contributions, in kcal mol^{-1}, for the first $H_2 + OH \longrightarrow H_2O + H$ reactive pathway, extracted from a larger MD simulation, are presented for the four ReaxFF parameter sets studied. The atom energy is the sum of the overcoordination and undercoordination energy contributions. The total time to complete this reaction path is 30 fs with a time step of 0.1 fs.

on a hydroperoxyl radical to form two hydroxyl radicals ($HO_2 + H \longrightarrow 2\,OH$) on the triplet surface, the abstraction of hydrogen from a hydroperoxyl radical by a second hydroperoxyl radical to form a hydrogen peroxide molecule and an oxygen molecule ($2\,HO_2 \longrightarrow H_2O_2 + O_2$) on the triplet surface, the radical attack of a hydrogen atom on a hydrogen peroxide molecule to form a water molecule and a hydroxyl radical ($H_2O_2 + H \longrightarrow H_2O + OH$) on the doublet surface, the abstraction of hydrogen from a hydrogen peroxide molecule by a hydrogen atom to form a hydrogen molecule and a hydroperoxyl radical ($H_2O_2 + H \longrightarrow H_2 + HO_2$) on the doublet surface, the abstraction of hydrogen from a hydrogen peroxide molecule by an oxygen atom to form a hydroperoxyl radical and a hydroxyl radical ($H_2O_2 + O \longrightarrow HO_2 + OH$) on the triplet surface, and the abstraction of hydrogen from a hydrogen peroxide molecule by a hydroxyl radical to form a water molecule and a hydroperoxyl radical ($H_2O_2 + OH \longrightarrow H_2O + HO_2$) on the doublet surface. Plots of the potential energy along the IRCs for the methods surveyed are presented in Figures 4,5,S8–S18.

Table 2 presents the RMSD, MSD, MAX, and NPE, all in kcal mol^{-1}, for the IRC scans. For the overall metrics, ωB97M-V again outperforms all of the surveyed ReaxFF methods by at least a factor of 4 for RMSDs, 5 for MAXs, and 6 for NPEs. Of the ReaxFF methods, the CHO2016 parameter set is shown to outperform all other parameter sets in terms of RMSDs with a value of 11.79 kcal mol^{-1}, followed closely by the HO2011 set the CHO2008 set, and finally the HO2014 set. For NPEs, the worst performances are 42.86 kcal mol^{-1}, 47.07 kcal mol^{-1}, 48.60 kcal mol^{-1}, and 59.91 kcal mol^{-1} for the CHO2008 set, the CHO2016 set, the HO2011 set, and the HO2014 set, respectively. The lowest NPE for any of the ReaxFF parameter sets is 12.53 kcal mol^{-1}. This demonstrates the failure of ReaxFF to quantitatively replicate the shape of the CCSD(T) potential energy surface.

Table 3 presents the reaction energies, forward reaction barrier heights, and reverse reaction barrier heights for the IRC scans at the CCSD(T)/CBS level of theory and errors in these quantities for all other methods considered. For these calculations, forward and reverse barrier heights are measured as the difference between the maximum along the IRC and the

15

Table 2: Root mean square deviation, mean signed deviation, maximum absolute deviation, and non-parallelity error, in kcal/mol, are presented for a selection of intrinsic reaction coordinate scans of elementary reactions relevant to hydrogen combustion. Geometries along the reaction coordinate were calculated at the ωB97M-V/cc-pVTZ level of theory. CCSD(T)/CBS values were used as reference.

Reaction	Method	RMSD	MSD	MAX	NPE
$H + O_2 \longrightarrow OH + O$	ωB97M-V	1.52	1.36	2.85	2.33
	CHO2008	12.40	-9.37	-37.57	34.64
	HO2011	16.62	-12.14	-42.34	39.11
	HO2014	14.38	-0.96	33.47	45.50
	CHO2016	17.33	-12.77	-48.72	43.71
$H_2 + OH \longrightarrow H_2O + H$	ωB97M-V	2.20	0.95	2.91	5.22
	CHO2008	6.40	2.22	-12.38	21.04
	HO2011	15.50	9.56	44.54	48.60
	HO2014	9.35	3.56	23.35	30.88
	CHO2016	9.24	5.54	16.31	23.16
$H_2O + O \longrightarrow 2\,OH$	ωB97M-V	4.03	-3.51	-6.72	5.73
	CHO2008	28.88	-25.50	-53.15	42.86
	HO2011	11.65	-4.05	23.24	39.46
	HO2014	17.63	-13.75	-31.44	36.48
	CHO2016	12.91	-10.61	-24.57	23.96
$H + O_2 \longrightarrow HO_2$	ωB97M-V	1.15	0.97	1.92	1.80
	CHO2008	10.25	-10.12	-14.06	6.76
	HO2011	9.40	-5.59	-14.17	21.20
	HO2014	14.92	-7.46	-21.49	36.32
	CHO2016	7.69	-2.68	-10.47	19.55
$HO_2 + H \longrightarrow H_2 + O_2$	ωB97M-V	1.08	-0.40	-3.23	3.98
	CHO2008	10.03	4.98	19.05	31.95
	HO2011	5.18	-2.59	-11.57	15.35
	HO2014	21.36	-17.28	-32.82	33.26
	CHO2016	6.18	-1.29	12.06	19.38
$HO_2 + H \longrightarrow 2\,OH$	ωB97M-V	2.38	1.87	4.04	3.68
	CHO2008	11.84	-9.93	-28.12	26.36
	HO2011	16.17	-6.87	-36.94	47.49
	HO2014	25.91	-21.95	-38.11	34.65
	CHO2016	17.39	-11.83	-49.89	47.07
$2\,HO_2 \longrightarrow H_2O_2 + O_2$	ωB97M-V	1.97	-0.69	-4.27	5.93
	CHO2008	5.31	-2.69	-15.33	22.31
	HO2011	12.00	10.01	24.65	23.63
	HO2014	25.32	-9.90	-41.68	59.91
	CHO2016	11.75	4.01	20.44	31.80
$H_2O_2 + H \longrightarrow H_2O + OH$	ωB97M-V	2.12	1.81	3.12	3.42
	CHO2008	3.81	1.83	11.49	12.53
	HO2011	12.96	9.26	19.18	20.57
	HO2014	16.97	5.62	41.82	50.24
	CHO2016	11.84	7.00	17.84	23.45
$H_2O_2 + H \longrightarrow H_2 + HO_2$	ωB97M-V	2.65	-1.59	-4.87	5.84
	CHO2008	6.49	-1.64	-17.13	22.76
	HO2011	9.05	5.78	30.34	37.39
	HO2014	9.61	5.88	16.51	22.95
	CHO2016	4.90	1.15	-11.22	17.91
$H_2O_2 + O \longrightarrow HO_2 + OH$	ωB97M-V	3.86	-3.37	-7.71	6.77
	CHO2008	19.71	-17.65	-38.11	30.37
	HO2011	9.66	2.29	26.85	32.55
	HO2014	7.82	2.69	20.47	25.41
	CHO2016	4.50	1.09	7.78	13.85
$H_2O_2 + OH \longrightarrow H_2O + HO_2$	ωB97M-V	2.68	-2.49	-6.79	4.88
	CHO2008	8.92	-3.27	-28.16	34.93
	HO2011	10.77	7.74	32.74	28.52
	HO2014	21.47	15.92	44.76	43.01
	CHO2016	13.27	8.13	22.78	25.31
All IRCs	ωB97M-V	2.49	-0.42	-7.71	6.77
	CHO2008	12.47	-5.54	-53.15	42.86
	HO2011	12.36	1.78	44.54	48.60
	HO2014	18.30	-2.46	44.76	59.91
	CHO2016	11.79	-0.40	-49.89	47.07

isolated reactants or products at the ωB97M-V/cc-pVTZ optimized geometries, respectively. Reaction energies are computed as the difference between these isolated products and reactants. For both reaction energies and barrier heights ωB97M-V outperforms the best ReaxFF methods by a factor of 2 for reaction energy errors and a factor of 3 for barrier height errors. Of the ReaxFF parameter sets, the HO2011 set shows the best performance for reaction energies with an RMSD of 7.15 kcal mol^{-1}, followed by the CHO2016 set, the CHO2008 set, and the HO2014 set with RMSDs of 12.40 kcal mol^{-1}, 14.67 kcal mol^{-1}, and 25.09 kcal mol^{-1}, respectively. Turning to barrier heights, the performance of the ReaxFF methods is split, with the CHO2008 and CHO2016 parameter sets outperforming the HO2014 and HO2011 parameter sets by more than 8 kcal mol^{-1}. The CHO2008 parameter set is generally seen to underestimate the forward and reverse barriers and in many cases stabilizes configurations in the region of the ωB97M-V transition state, leading to a double-barrier potential energy surface. The CHO2016 parameter set shows a similar performance, both underestimating forward and reverse barriers and exhibiting multiple barriers on the potential energy surface. For the HO2011 parameter set, forward and reverse barriers are seen to be overestimated on average. In particular, reaction barriers are strongly overestimated for hydrogen transfer reactions, with the exception of the $\text{HO}_2 + \text{H} \longrightarrow \text{H}_2 + \text{O}_2$ IRC scan. The HO2014 parameter set also overestimates both forward and reverse reaction barriers on average, with the performance being exacerbated by the poor performance on reaction energies.

Figure 4 presents the potential energy along the $\text{H}_2 + \text{OH} \longrightarrow \text{H}_2\text{O} + \text{H}$ IRC for the CCSD(T) reference, ωB97M-V, and the four ReaxFF parameter sets. For the CHO2008 parameter set, we see a slightly overestimated barrier followed by a overstabilization of the configurations in the center of the scan. The HO2011 parameter set is seen to overestimate the forward and reverse barriers by 34 kcal mol^{-1} and 25 kcal mol^{-1}, respectively. The HO2014 parameter set exhibits an exaggerated forward barrier and underestimates the stabilization in the product channel. The CHO2016 parameter set yields a comparatively good forward barrier but clearly overstabilizes configurations near the transition state leading to

17

Table 3: Reaction energy errors, forward reaction barrier height errors, and reverse reaction barrier height errors, in kcal mol^{-1}, are presented for a selection of intrinsic reaction coordinate scans of elementary reactions relevant to hydrogen combustion. Geometries along the reaction coordinate were calculated at the ωB97M-V/cc-pVTZ level of theory. CCSD(T)/CBS values were used as a reference and the reaction energies, forward reaction barriers, and reverse reaction barriers are reported, in kcal mol^{-1}. Infinitely separated reactants and products optimized at the ωB97M-V/cc-pVTZ level of theory are taken as the endpoints of the reaction paths.

Reaction	Method	ΔE	$\Delta E_f^{\ddagger}$	$\Delta E_b^{\ddagger}$
$H + O_2 \longrightarrow OH + O$	CCSD(T)/CBS	11.73	41.05	29.32
	ωB97M-V	5.51	2.69	-2.82
	CHO2008	-17.22	-20.15	-2.92
	HO2011	6.43	-35.80	-42.23
	HO2014	-13.00	13.59	26.58
	CHO2016	-5.99	-33.38	-27.39
$H_2 + OH \longrightarrow H_2O + H$	CCSD(T)/CBS	-16.63	5.61	22.24
	ωB97M-V	2.05	-2.31	-4.36
	CHO2008	8.55	3.27	-5.28
	HO2011	8.64	34.06	25.42
	HO2014	9.15	10.74	1.58
	CHO2016	13.62	2.72	-10.90
$H_2O + O \longrightarrow 2\,OH$	CCSD(T)/CBS	19.00	22.05	3.06
	ωB97M-V	-1.92	-6.65	-4.73
	CHO2008	-25.83	-32.91	-7.08
	HO2011	-13.82	21.44	35.26
	HO2014	-28.01	1.69	29.70
	CHO2016	-16.88	-13.76	3.12
$H + O_2 \longrightarrow HO_2$	CCSD(T)/CBS	-55.81	1.56	57.37
	ωB97M-V	1.48	0.23	-1.25
	CHO2008	-14.25	-7.54	6.70
	HO2011	7.00	-7.98	-14.98
	HO2014	15.24	-16.32	-31.56
	CHO2016	5.61	-7.30	-12.91
$HO_2 + H \longrightarrow H_2 + O_2$	CCSD(T)/CBS	-54.12	2.62	56.74
	ωB97M-V	-0.17	-0.95	-0.78
	CHO2008	18.37	-2.85	-21.21
	HO2011	0.02	1.15	1.13
	HO2014	-13.89	-0.94	12.95
	CHO2016	-0.09	7.84	7.94
$HO_2 + H \longrightarrow 2\,OH$	CCSD(T)/CBS	-40.02	14.42	54.43
	ωB97M-V	5.46	0.95	-4.52
	CHO2008	-16.15	-15.79	0.35
	HO2011	1.26	-15.54	-16.79
	HO2014	-45.75	-8.68	37.07
	CHO2016	-9.34	-16.70	-7.36
$2\,HO_2 \longrightarrow H_2O_2 + O_2$	CCSD(T)/CBS	-39.20	0.29	39.49
	ωB97M-V	2.75	-4.00	-6.75
	CHO2008	10.76	-11.09	-21.84
	HO2011	-0.19	20.58	20.77
	HO2014	-38.29	17.53	55.81
	CHO2016	-10.53	17.04	27.57
$H_2O_2 + H \longrightarrow H_2O + OH$	CCSD(T)/CBS	-71.56	7.19	78.76
	ωB97M-V	4.59	0.08	-4.51
	CHO2008	0.01	10.06	10.05
	HO2011	10.10	2.00	-8.10
	HO2014	-12.20	29.67	41.87
	CHO2016	14.72	-5.41	-20.14
$H_2O_2 + H \longrightarrow H_2 + HO_2$	CCSD(T)/CBS	-14.92	10.24	25.16
	ωB97M-V	-2.92	-3.23	-0.31
	CHO2008	7.61	-9.55	-17.16
	HO2011	0.20	28.29	28.09
	HO2014	24.40	3.89	-20.51
	CHO2016	10.44	-2.17	-12.62
$H_2O_2 + O \longrightarrow HO_2 + OH$	CCSD(T)/CBS	-12.55	11.86	24.42
	ωB97M-V	-2.79	-7.29	-4.50
	CHO2008	-9.67	-21.31	-11.64
	HO2011	-4.98	24.35	29.33
	HO2014	5.54	10.19	4.65
	CHO2016	7.18	-2.10	-9.29
$H_2O_2 + OH \longrightarrow H_2O + HO_2$	CCSD(T)/CBS	-31.55	3.33	34.88
	ωB97M-V	-0.87	-5.69	-4.81
	CHO2008	16.16	-10.66	-26.82
	HO2011	8.84	26.29	17.46
	HO2014	33.55	25.20	-8.35
	CHO2016	24.06	1.77	-22.29
RMSD	ωB97M-V	3.25	4.00	
	CHO2008	14.67	15.08	
	HO2011	7.15	23.69	
	HO2014	25.09	23.45	
	CHO2016	12.40	15.24	

18

a second barrier.

Figure 5 presents the potential energy along the $H_2O_2 + OH \longrightarrow H_2O + HO_2$ IRC for the CCSD(T) reference, ωB97M-V, and the four ReaxFF parameter sets. Here the CHO2008 parameter set fails to predict a forward barrier to reaction and significantly overstabilizes configuration in the transition state regime. The HO2011 parameter set yields an exaggerated barrier that overestimates the forward barrier height by 26 kcal mol^{-1} and the reverse barrier height by 17 kcal mol^{-1}. For the HO2014 parameter set the forward barrier is exaggerated nearly to the extent of the HO2011 parameter set and severely understabilizes the product channel, leading to a reaction energy error of 34 kcal mol^{-1}. The CHO2016 parameter set again gives a second barrier for this reaction and poorly reproduces the reaction barrier.
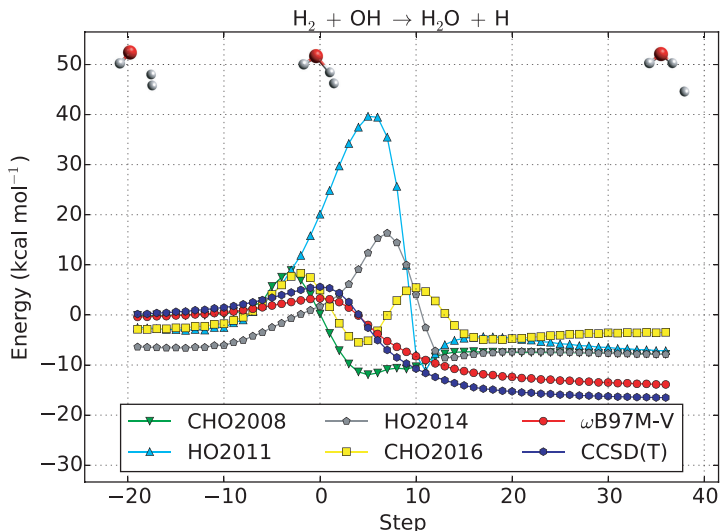
Figure 4: Potential energies along the $H_2 + OH \longrightarrow H_2O + H$ intrinsic reaction coordinate are presented for four ReaxFF parameter sets, ωB97M-V, and CCSD(T). Geometries along the reaction coordinate were calculated at the ωB97M-V/cc-pVTZ level of theory. The energies presented are relative to the energies of isolated H_2 and OH computed at the ωB97M-V/cc-pVTZ optimized geometries.

For both of the reactions presented above, Agrawalla and van Duin[54] show that the forward reactions should have no forward barrier with the HO2011 parameter set. In order to better elucidate the nature of the potential energy surfaces, Figures 6 and 7 present unrelaxed two-dimensional potential energy surfaces for the reactions $H_2 + OH \longrightarrow H_2O + H$

19

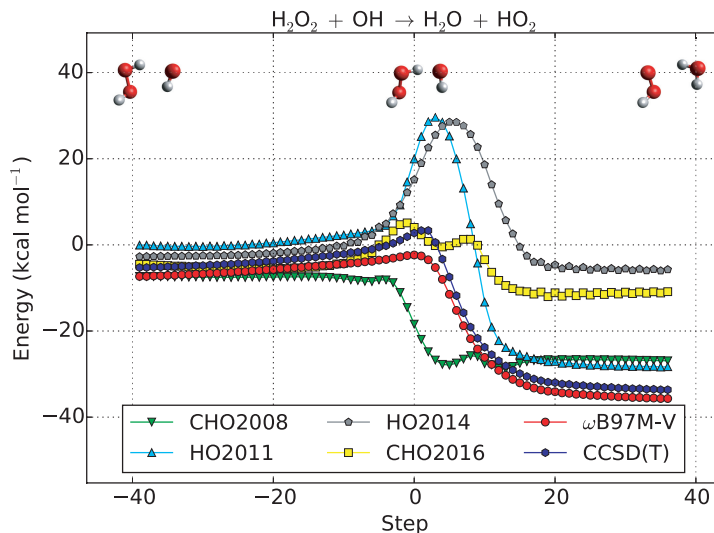Figure 5: Potential energies along the $H_2O_2 + OH \longrightarrow H_2O + HO_2$ intrinsic reaction coordinate are presented for four ReaxFF parameter sets, ωB97M-V, and CCSD(T). Geometries along the reaction coordinate were calculated at the ωB97M-V/cc-pVTZ level of theory. The energies presented are relative to the energies of isolated H_2O_2 and OH computed at the ωB97M-V/cc-pVTZ optimized geometries.

and $H_2O_2 + OH \longrightarrow H_2O + HO_2$, respectively. For these surfaces, the bonds which are breaking and forming are linearized while all other internal coordinates are held fixed in the configuration of the transition state calculated at the ωB97M-V/cc-pVTZ level of theory. The interatomic distance along the IRC for the bonds breaking and forming are superimposed in each plot to approximate the one-dimensional slices given in Figures 4 and 5.

Beginning with $H_2 + OH \longrightarrow H_2O + H$, the transition state structure as optimized with ωB97M-V has an HO$-$H bond length of 1.35 Å and a H$-$H bond length of 0.82 Å. The CHO2008 surface displays an entrance channel with a longer optimal H$-$H bond length and predicts a transition state structure to occur with a longer HO$-$H bond length and a longer H$-$H bond length. This surface also displays a well that extends to much shorter H$-$H bond lengths than the ωB97M-V surface. The HO2011 surface predicts a transition state structure with a longer H$-$H bond length. Following the IRC on the HO2011 surface elucidates the origin of the large errors in the barrier heights for this parameter set. The HO2014 surface predicts a transition state structure with a longer H$-$H bond length while
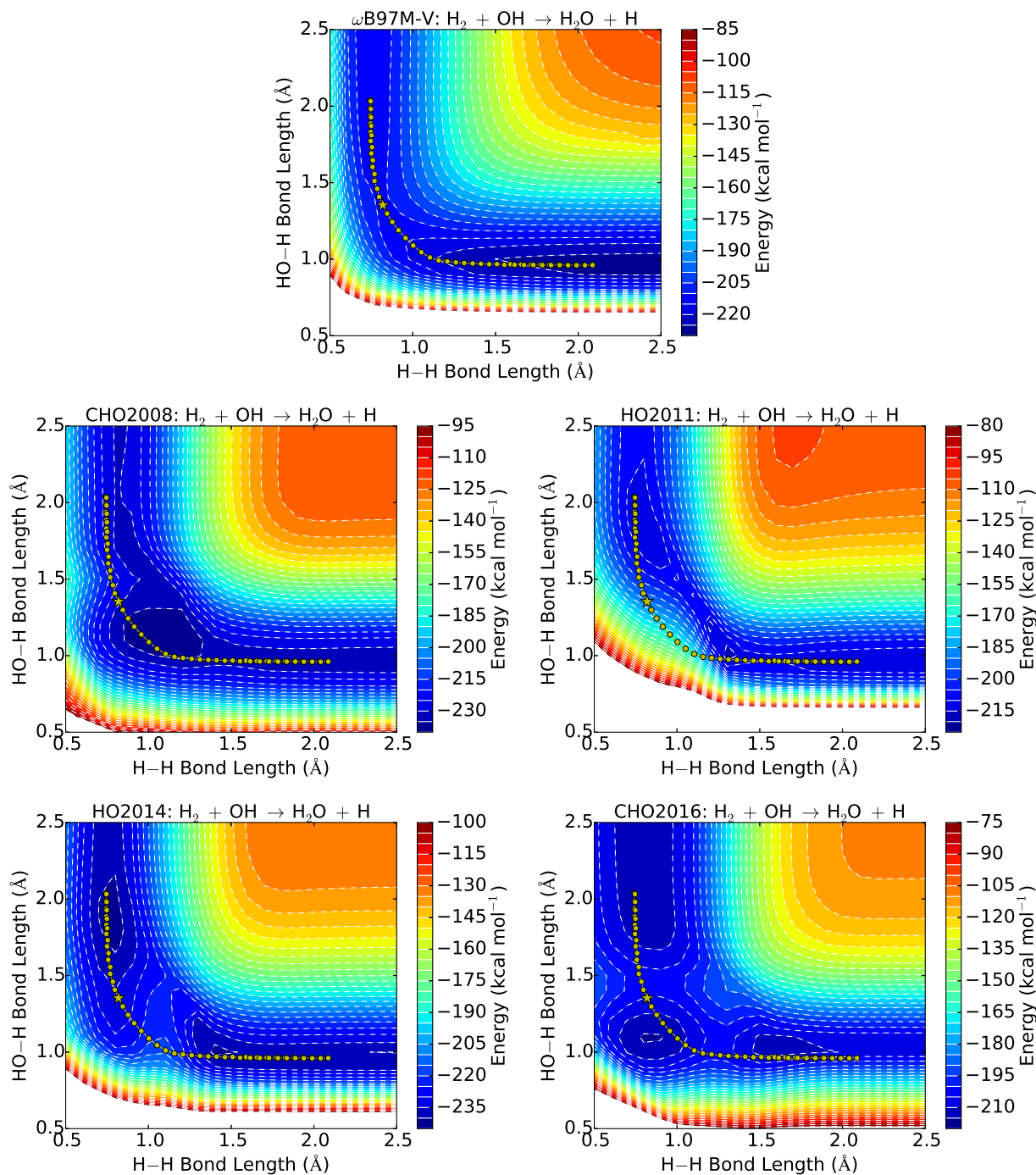
20

Figure 6: Unrelaxed potential energy surfaces for the $H_2 + OH \longrightarrow H_2O + H$ reaction, in kcal mol^{-1}, are presented for ωB97M-V and four ReaxFF parameter sets. Here the HO···H···H angle is linearized while all other geometric parameters are held fixed in the transitions state configuration as optimized at the ωB97M-V/cc-pVTZ level of theory. The interatomic distances for points along the intrinsic reaction coordinate calculated at the ωB97M-V/cc-pVTZ level of theory are overlaid on each surface. The energies presented are relative to the energies of the isolated atoms.

the IRC skews toward a longer HO−H bond length, leading to an exaggerated barrier. The CHO2016 surface demonstrates the double barrier seen in Figure 4, with one transition state structure with a longer HO−H bond length and another with a longer H−H bond length. This surface also exhibits an exit channel with a slightly longer HO−H bond length than the ωB97M-V surface.

For $H_2O_2+OH \longrightarrow H_2O+HO_2$, the transition state structure as optimized with ωB97M-V has an HOO−H bond length of 1.04 Å and a HO−H bond length of 1.37 Å. The CHO2008 surface exhibits a transition state structure with a longer HO−H bond length and a well in the region immediately after the ωB97M-V transition state. The HO2011 surface predicts a transition state structure with a longer HOO−H bond length, leading to an exaggeration of the barrier along the ωB97M-V IRC. This behavior is also seen in the HO2014 surface, though the HO2014 surface predicts a longer optimum HOO−H bond length in the entrance channel. The CHO2016 surface exhibits very little energy variation across the IRC, which misses a narrow well in the product channel. The IRC is also destabilized by a short HOO−H bond length in the region of the ωB97M-V transition state.

These two dimensional potential energy surfaces, coupled with the IRC scans, demonstrate failures of the ReaxFF methods to accurately model the QM methods. The ReaxFF potential show a general trend towards looser transition state structures. These differences can be expected to manifest themselves in MD simulations, where exaggerated barriers will prevent reactivity that would otherwise occur on the QM surfaces and under-estimated barriers will overrepresent other reactions.

Conclusions

We have benchmarked the performance of several ReaxFF methods against state-of-the-art DFT calculations and CCSD(T). The data sets included both reactive pathways extracted from MD simulations and IRC scans, reaction energies, and barrier heights computed with
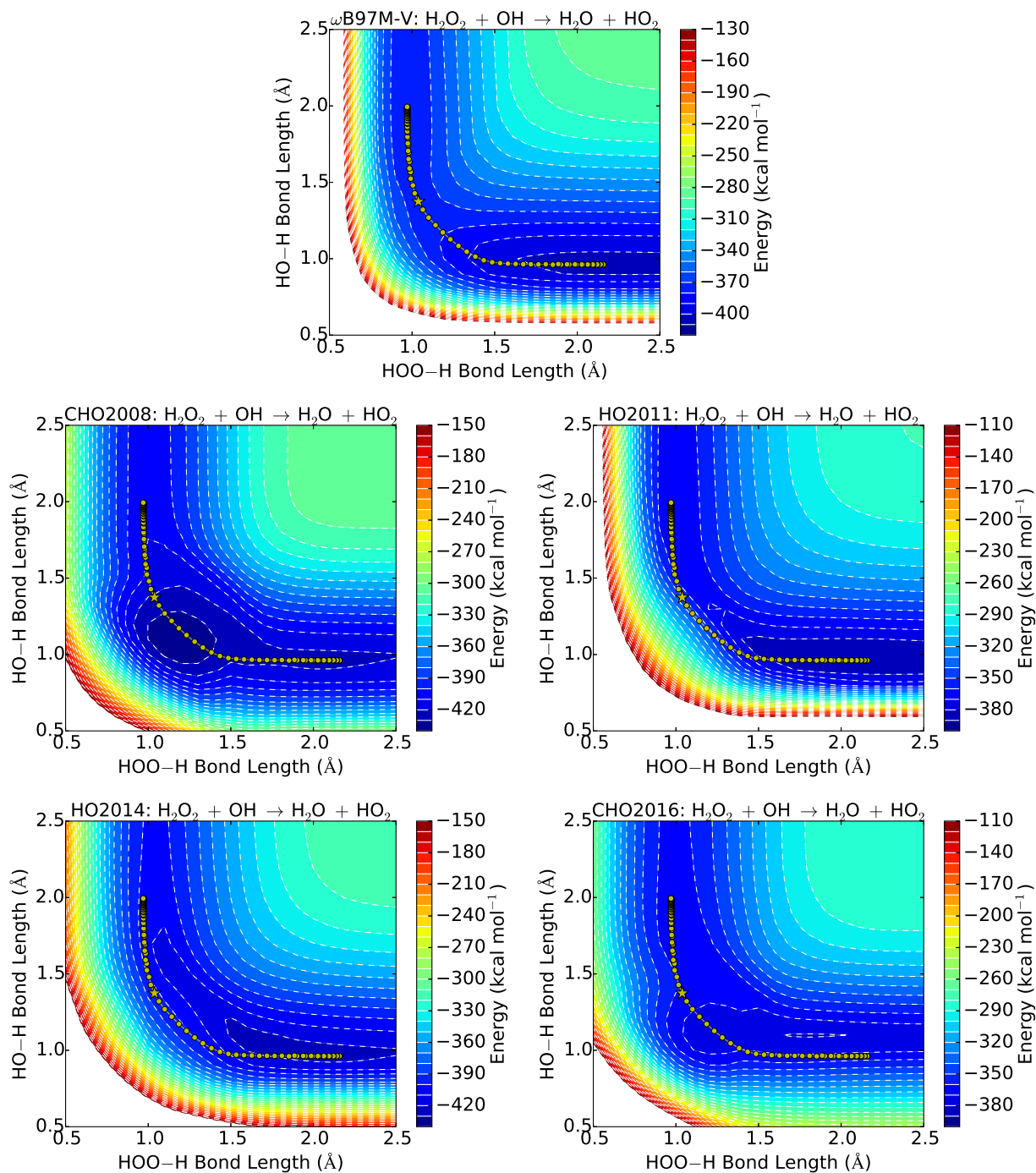
Figure 7: Unrelaxed potential energy surfaces for the $H_2O_2 + OH \longrightarrow H_2O + HO_2$ reaction, in kcal mol^{-1}, are presented for ωB97M-V and four ReaxFF parameter sets. Here the HOO···H···OH angle is linearized while all other geometric parameters are held fixed in the transitions state configuration as optimized at the ωB97M-V/cc-pVTZ level of theory. The interatomic distances for points along the intrinsic reaction coordinate calculated at the ωB97M-V/cc-pVTZ level of theory are overlaid on each surface. The energies presented are relative to the energies of the isolated atoms.

ωB97M-V. For the reactive pathways, the CHO2016 and HO2011 parameter sets had the best RMSDs (11 and 12 kcal mol^{-1}, respectively) while the average NPEs were similar across all methods surveyed (38 kcal mol^{-1}, 40 kcal mol^{-1}, 42 kcal mol^1, and 42 kcal mol^{-1} for CHO2008, HO2011, HO2014, and CHO2016, respectively). Along the reaction coordinate scans, the CHO2016, HO2011, and CHO2008 parameter sets exhibit similar performance on RMSDs (12 kcal mol^{-1}), while the average NPEs are favor CHO2008 and CHO2016 (26 kcal mol^{-1} for CHO2008 and CHO2016; 32 kcal mol^{-1} and 38 kcal mol^{-1} for HO2011 and HO2014, respectively). While in principle the RMSDs are subject to systematic error, the NPEs serve as an independent metric.

While these results appear to be a condemnation of ReaxFF methods for these systems, studies by both the developers[39,51–55,57,58,61,63,67–72,74,76–81,83–97] and users[31–34,56,59,60,62,64–66,73,75,82] have demonstrated the utility of ReaxFF as an exploratory tool for atomistic simulation. We also acknowledge the difficulty of parameter training for the ReaxFF system. Our results here point to ways to improve the treatment of hydrogen combustion.

- Amount of training data: Training data for the hydrogen combustion potentials with ReaxFF has largely centered around bond stretches, angle distortions, heats of formation, and reaction barriers. As seen in the IRC scans, the transition state structures computed with DFT are often higher-energy structures on the ReaxFF potential energy surfaces. More geometric properties of transition state structures in the ReaxFF training set should in principle help to relieve this discrepancy. The variable performance of the various ReaxFF potentials on the reactive pathways suggest that inclusion of data points far from the minimum energy pathways would improve the overall fidelity of the method.

- Quality of training data: References 51, 54, and 67 all specify that the QM training data was generated at the B3LYP/6-311G** level of theory.[119–121] A recent review of DFT benchmarked the performance of over 200 functionals across diverse chemical systems, including hydrogen transfer and non-hydrogen transfer barrier heights. For

these two test sets, B3LYP gave RMSDs of 4.89 kcal mol^{-1} and 5.52 kcal mol^{-1}, respectively, while ωB97M-V gave RMSDs of 1.72 kcal mol^{-1} and 1.98 kcal mol^{-1}, respectively.

- Optimization methods for parameter training: The ReaxFF parameter sets employed in this study were generated using the successive one-parameter parabolic extrapolation (SOPPE) approach,[122] which is both tedious and subject to converging to local minima. As a more global optimization scheme, several studies beginning with Pahari and Chaturvedi in 2012[123] and Larrson, van Duin, and Hartke[124,125] in 2013 have used genetic algorithms to optimize parameters for different ReaxFF potentials. More recently, a study of ReaxFF parameter optimization with Monte-Carlo and evolutionary algorithms has shown that care needs to be used when employing such methods and gives recommendations for initial guesses.[126] Machine learning approaches have also been applied recently to a parameter optimization scheme for ReaxFF[127]

- Overall form of the potential: Furman and Wales[128] recently published a letter in which a Taper corrections applied to bond order and bond length terms in ReaxFF are able to greatly reduce energy drifts seen in MD simulations on long timescales. Such corrections could in principle improve the sharp changes in the atom energy term seen in Figure 3. Currently work is also being done to replace the charge equilibration scheme in ReaxFF with a more advanced C-GeM model.[129]

Overall, the benchmarking of ReaxFF potential for hydrogen combustion systems shows that there is room for improvement in order to more closely match QM potential energies, energy differences important for thermochemistry, and energy barriers controlling chemical kinetics.

Acknowledgement

Supporting Information Available

Coordinates along the reactive pathways and IRC are available from the authors upon request. Plots of the potential energies along the pathways and IRCs are presented for all methods surveyed.

References

(1) Dawson, V. P.; Bowles, M. D. *Taming Liquid Hydrogen: The Centaur Upper Stage Rocket*; National Aeronautics and Space Administration, Office of External Relations: Washington, DC, 2004.

(2) Schlapbach, L.; Züttel, A. Hydrogen-storage materials for mobile applications. *Nature* **2001**, *414*, 353–358.

(3) Schlapbach, L. Technology: Hydrogen-fuelled vehicles. *Nature* **2009**, *460*, 809.

(4) Verhelst, S.; Wallner, T. Hydrogen-fueled internal combustion engines. *Prog. Energy Combust. Sci.* **2009**, *35*, 490–527.

(5) Chu, S.; Majumdar, A. Opportunities and challenges for a sustainable energy future. *Nature* **2012**, *488*, 294.

(6) Marbán, G.; Valdás-Solís, T. Towards the hydrogen economy? *Int. J. Hydrog. Energy* **2007**, *32*, 1625 – 1637.

(7) Midilli, A.; Dincer, I. Hydrogen as a renewable and sustainable solution in reducing global fossil fuel consumption. *Int. J. Hydrog. Energy* **2008**, *33*, 4209–4222.

(8) Sánchez, A. L.; Williams, F. A. Recent advances in understanding of flammability characteristics of hydrogen. *Prog. Energy Combust. Sci.* **2014**, *41*, 1 – 55.

(9) Palumbo, O.; Paolone, A.; Rispoli, P.; Cantelli, R. Novel materials for solid-state hydrogen storage: Anelastic spectroscopy studies. *Mater. Sci. Eng. A* **2009**, *521*, 134–138.

(10) Petukhov, V. A.; Naboko, I. M.; Fortov, V. E. Explosion hazard of hydrogen–air mixtures in the large volumes. *Int. J. Hydrog. Energy* **2009**, *34*, 5924–5931.

(11) Ray, I.; Chakraborty, T.; Roy, D.; Datta, A.; Mandal, B. K. Production, storage and properties of hydrogen as internal combustion engine fuel: a critical review. *Int. J. Emerging Technol. Adv. Eng.* **2013**, *3*, 119–125.

(12) Verhelst, S. Recent progress in the use of hydrogen as a fuel for internal combustion engines. *Int. J. Hydrog. Energy* **2014**, *39*, 1071–1085.

(13) Allendorf, M. D.; Hulvey, Z.; Gennett, T.; Ahmed, A.; Autrey, T.; Camp, J.; Cho, E. S.; Furukawa, H.; Haranczyk, M.; Head-Gordon, M., et al. An assessment of strategies for the development of solid-state adsorbents for vehicular hydrogen storage. *Energy Environ. Sci.* **2018**, *11*, 2784–2812.

(14) Boivin, P.; Sánchez, A. L.; Williams, F. A. Analytical prediction of syngas induction times. *Combust. Flame* **2017**, *176*, 489 – 499.

(15) Mueller, M. A.; Kim, T. J.; Yetter, R. A.; Dryer, F. L. Flow reactor studies and kinetic modeling of the H_2/O_2 reaction. *Int. J. Chem. Kinet.* **1999**, *31*, 113–125.

(16) Li, J.; Zhao, Z.; Kazakov, A.; Dryer, F. L. An updated comprehensive kinetic model of hydrogen combustion. *Int. J. Chem. Kinet.* **2004**, *36*, 566–575.

(17) O'Conaire, M.; Curran, H. J.; Simmie, J. M.; Pitz, W. J.; Westbrook, C. K. A comprehensive modeling study of hydrogen oxidation. *Int. J. Chem. Kinet.* **2004**, *36*, 603–622.

(18) Konnov, A. A. Remaining uncertainties in the kinetic mechanism of hydrogen combustion. *Combust. Flame* **2008**, *152*, 507–528.

(19) Hong, Z.; Davidson, D. F.; Hanson, R. K. An improved H_2/O_2 mechanism based on recent shock tube/laser absorption measurements. *Combust. Flame* **2011**, *158*, 633–644.

(20) Burke, M. P.; Chaos, M.; Ju, Y.; Dryer, F. L.; Klippenstein, S. J. Comprehensive H_2/O_2 kinetic model for high-pressure combustion. *Int. J. Chem. Kinet.* **2012**, *44*, 444–474.

(21) Shimizu, K.; Hibi, A.; Koshi, M.; Morii, Y.; Tsuboi, N. Updated kinetic mechanism for high-pressure hydrogen combustion. *J. Propul. Power* **2011**, *27*, 383–395.

(22) Kitano, S.; Fukao, M.; Susa, A.; Tsuboi, N.; Hayashi, A.; Koshi, M. Spinning detonation and velocity deficit in small diameter tubes. *Proc. Combust. Inst.* **2009**, *32*, 2355–2362.

(23) Varga, T.; Nagy, T.; Olm, C.; Zsély, I. G.; Pálvölgyi, R.; Valkó, É.; Vincze, G.; Cserháti, M.; Curran, H.; Turányi, T. Optimization of a hydrogen combustion mechanism using both direct and indirect measurements. *Proc. Combust. Inst.* **2015**, *35*, 589–596.

(24) Yang, S.; Yang, X.; Wu, F.; Ju, Y.; Law, C. K. Laminar flame speeds and kinetic modeling of H_2/O_2/diluent mixtures at sub-atmospheric and elevated pressures. *Proc. Combust. Inst.* **2017**, *36*, 491–498.

(25) Burke, M. P.; Klippenstein, S. J. Ephemeral collision complexes mediate chemically termolecular transformations that affect system chemistry. *Nat. Chem.* **2017**, *9*, 1078–1082.

(26) Konnov, A. A. Yet another kinetic mechanism for hydrogen combustion. *Combust. Flame* **2019**, *203*, 14–22.

(27) Jasper, A. W.; Kamarchik, E.; Miller, J. A.; Klippenstein, S. J. First-principles binary diffusion coefficients for H, H_2, and four normal alkanes $+$ N_2. *J. Chem. Phys.* **2014**, *141*, 124313.

(28) Jasper, A. W.; Miller, J. A. Lennard–Jones parameters for combustion and chemical kinetics modeling from full-dimensional intermolecular potentials. *Combust. Flame* **2014**, *161*, 101–110.

(29) Mulvihill, C. R.; Petersen, E. L. Concerning shock-tube ignition delay times: an experimental investigation of impurities in the H_2/O_2 system and beyond. *Proc. Combust. Inst.* **2019**, *37*, 259–266.

(30) Sabia, P.; de Joannon, M. On H_2–O_2 oxidation in several bath gases. *Int. J. Hydrog. Energy* **2020**, *45*, 8151–8167.

(31) Alaghemandi, M.; Green, J. R. Reactive symbol sequences for a model of hydrogen combustion. *Phys. Chem. Chem. Phys.* **2016**, *18*, 2810–2817.

(32) Alaghemandi, M.; Newcomb, L. B.; Green, J. R. Ignition in an atomistic model of hydrogen oxidation. *J. Phys. Chem. A* **2017**, *121*, 1686–1692.

(33) Nicholson, S. B.; Alaghemandi, M.; Green, J. R. Learning the mechanisms of chemical disequilibria. *J. Chem. Phys.* **2016**, *145*, 084112.

(34) Nicholson, S. B.; Alaghemandi, M.; Green, J. R. Effects of temperature and mass

conservation on the typical chemical sequences of hydrogen oxidation. *J. Chem. Phys.* **2018**, *148*, 044102.

(35) Newcomb, L. B.; Alaghemandi, M.; Green, J. R. Nonequilibrium phase coexistence and criticality near the second explosion limit of hydrogen combustion. *J. Chem. Phys.* **2017**, *147*, 034108.

(36) Newcomb, L. B.; Marucci, M. E.; Green, J. R. Explosion limits of hydrogen–oxygen mixtures from nonequilibrium critical points. *Phys. Chem. Chem. Phys.* **2018**, *20*, 15746–15752.

(37) Warnatz, J. Resolution of gas phase and surface combustion chemistry into elementary reactions. Symp. (Int.) Combust. 1992; pp 553–579.

(38) Van de Vijver, R.; Vandewiele, N. M.; Bhoorasingh, P. L.; Slakman, B. L.; Seyedzadeh Khanshan, F.; Carstensen, H.-H.; Reyniers, M.-F.; Marin, G. B.; West, R. H.; Van Geem, K. M. Automatic Mechanism and Kinetic Model Generation for Gas-and Solution-Phase Processes: A Perspective on Best Practices, Recent Advances, and Future Challenges. *Int. J. Chem. Kinet.* **2015**, *47*, 199–231.

(39) Van Duin, A. C.; Dasgupta, S.; Lorant, F.; Goddard, W. A. ReaxFF: a reactive force field for hydrocarbons. *J. Phys. Chem. A* **2001**, *105*, 9396–9409.

(40) Wang, L.-P.; Titov, A.; McGibbon, R.; Liu, F.; Pande, V. S.; Martínez, T. J. Discovering chemistry with an ab initio nanoreactor. *Nat. Chem.* **2014**, *6*, 1044.

(41) Martínez, T. J. Ab Initio Reactive Computer Aided Molecular Design. *Acc. Chem. Res.* **2017**, *50*, 652–656.

(42) Brenner, D. W. Empirical potential for hydrocarbons for use in simulating the chemical vapor deposition of diamond films. *Phys. Rev. B* **1990**, *42*, 9458.

(43) Brenner, D. W.; Shenderova, O. A.; Harrison, J. A.; Stuart, S. J.; Ni, B.; Sinnott, S. B. A second-generation reactive empirical bond order (REBO) potential energy expression for hydrocarbons. *J. Phys. Condens. Matter* **2002**, *14*, 783.

(44) Yu, J.; Sinnott, S. B.; Phillpot, S. R. Charge optimized many-body potential for the Si/SiO$_2$ system. *Phys. Rev. B* **2007**, *75*, 085311.

(45) Zhao, M.; Iron, M. A.; Staszewski, P.; Schultz, N. E.; Valero, R.; Truhlar, D. G. Valence–bond order (VBO): A new approach to modeling reactive potential energy surfaces for complex systems, materials, and nanoparticles. *J. Chem. Theory Comput.* **2009**, *5*, 594–604.

(46) Shan, T.-R.; Devine, B. D.; Hawkins, J. M.; Asthagiri, A.; Phillpot, S. R.; Sinnott, S. B. Second-generation charge-optimized many-body potential for Si/SiO$_2$ and amorphous silica. *Phys. Rev. B* **2010**, *82*, 235302.

(47) Nouranian, S.; Tschopp, M. A.; Gwaltney, S. R.; Baskes, M. I.; Horstemeyer, M. F. An interatomic potential for saturated hydrocarbons based on the modified embedded-atom method. *Phys. Chem. Chem. Phys.* **2014**, *16*, 6233–6249.

(48) Slater, J. C.; Koster, G. F. Simplified LCAO method for the periodic potential problem. *Phys. Rev.* **1954**, *94*, 1498.

(49) Andersen, O. K.; Jepsen, O. Explicit, first-principles tight-binding theory. *Phys. Rev. Lett.* **1984**, *53*, 2571.

(50) Bannwarth, C.; Ehlert, S.; Grimme, S. GFN2-xTB—An accurate and broadly parametrized self-consistent tight-binding quantum chemical method with multipole electrostatics and density-dependent dispersion contributions. *J. Chem. Theory Comput.* **2019**, *15*, 1652–1671.

(51) Chenoweth, K.; Van Duin, A. C. T.; Goddard, W. A. ReaxFF reactive force field for molecular dynamics simulations of hydrocarbon oxidation. *J. Phys. Chem. A* **2008**, *112*, 1040–1053.

(52) Chenoweth, K.; Van Duin, A. C. T.; Dasgupta, S.; Goddard III, W. A. Initiation mechanisms and kinetics of pyrolysis and combustion of JP-10 hydrocarbon jet fuel. *J. Phys. Chem. A* **2009**, *113*, 1740–1746.

(53) Weismiller, M. R.; van Duin, A. C. T.; Lee, J.; Yetter, R. A. ReaxFF Reactive Force Field Development and Applications for Molecular Dynamics Simulations of Ammonia Borane Dehydrogenation and Combustion. *J. Phys. Chem. A* **2010**, *114*, 5485–5492.

(54) Agrawalla, S.; Van Duin, A. C. T. Development and application of a ReaxFF reactive force field for hydrogen combustion. *J. Phys. Chem. A* **2011**, *115*, 960–972.

(55) Liu, L.; Bai, C.; Sun, H.; Goddard III, W. A. Mechanism and kinetics for the initial steps of pyrolysis and combustion of 1, 6-dicyclopropane-2, 4-hexyne from ReaxFF reactive dynamics. *J. Phys. Chem. A* **2011**, *115*, 4941–4950.

(56) Wang, Q.-D.; Wang, J.-B.; Li, J.-Q.; Tan, N.-X.; Li, X.-Y. Reactive molecular dynamics simulation and chemical kinetic modeling of pyrolysis and combustion of n-dodecane. *Combust. Flame* **2011**, *158*, 217–226.

(57) Qian, H.-J.; Van Duin, A. C. T.; Morokuma, K.; Irle, S. Reactive molecular dynamics simulation of fullerene combustion synthesis: ReaxFF vs DFTB potentials. *J. Chem. Theory Comput.* **2011**, *7*, 2040–2048.

(58) Castro-Marcano, F.; Kamat, A. M.; Russo Jr, M. F.; van Duin, A. C. T.; Mathews, J. P. Combustion of an Illinois No. 6 coal char simulated using an atomistic char representation and the ReaxFF reactive force field. *Combust. Flame* **2012**, *159*, 1272–1285.

(59) Cheng, X.-M.; Wang, Q.-D.; Li, J.-Q.; Wang, J.-B.; Li, X.-Y. ReaxFF molecular dynamics simulations of oxidation of toluene at high temperatures. *J. Phys. Chem. A* **2012**, *116*, 9811–9818.

(60) Guo, F.; Cheng, X.; Zhang, H. ReaxFF molecular dynamics study of initial mechanism of JP-10 combustion. *Combust. Sci. Technol.* **2012**, *184*, 1233–1243.

(61) Castro-Marcano, F.; van Duin, A. C. T. Comparison of thermal and catalytic cracking of 1-heptene from ReaxFF reactive molecular dynamics simulations. *Combust. Flame* **2013**, *160*, 766–775.

(62) Beste, A. ReaxFF study of the oxidation of lignin model compounds for the most common linkages in softwood in view of carbon fiber production. *J. Phys. Chem. A* **2014**, *118*, 803–814.

(63) Cheng, T.; Jaramillo-Botero, A.; Goddard III, W. A.; Sun, H. Adaptive accelerated ReaxFF reactive dynamics with validation from simulating hydrogen combustion. *J. Amer. Chem. Soc.* **2014**, *136*, 9434–9442.

(64) He, Z.; Li, X.-B.; Liu, L.-M.; Zhu, W. The intrinsic mechanism of methane oxidation under explosion condition: A combined ReaxFF and DFT study. *Fuel* **2014**, *124*, 85–90.

(65) Bharti, A.; Banerjee, T. Reactive force field simulation studies on the combustion behavior of n-octanol. *Fuel Process. Technol.* **2016**, *152*, 132–139.

(66) Zhang, T.; Li, X.; Qiao, X.; Zheng, M.; Guo, L.; Song, W.; Lin, W. Initial mechanisms for an overall behavior of lignin pyrolysis through large-scale ReaxFF molecular dynamics simulations. *Energy Fuels* **2016**, *30*, 3140–3150.

(67) Ashraf, C.; van Duin, A. C. T. Extension of the ReaxFF Combustion Force Field

toward Syngas Combustion and Initial Oxidation Kinetics. *J. Phys. Chem. A* **2017**, *121*, 1051–1068.

(68) Strachan, A.; van Duin, A. C. T.; Chakraborty, D.; Dasgupta, S.; Goddard III, W. A. Shock waves in high-energy materials: The initial chemical events in nitramine RDX. *Phys. Rev. Lett.* **2003**, *91*, 098301.

(69) Strachan, A.; Kober, E. M.; Van Duin, A. C. T.; Oxgaard, J.; Goddard III, W. A. Thermal decomposition of RDX from reactive molecular dynamics. *J. Chem. Phys.* **2005**, *122*, 054502.

(70) Buehler, M. J.; Van Duin, A. C. T.; Goddard III, W. A. Multiparadigm modeling of dynamical crack propagation in silicon using a reactive force field. *Phys. Rev. Lett.* **2006**, *96*, 095505.

(71) Ludwig, J.; Vlachos, D. G.; Van Duin, A. C. T.; Goddard, W. A. Dynamics of the dissociation of hydrogen on stepped platinum surfaces using the ReaxFF reactive force field. *J. Phys. Chem. B* **2006**, *110*, 4274–4282.

(72) Nomura, K.-i.; Kalia, R. K.; Nakano, A.; Vashishta, P.; Van Duin, A. C. T.; Goddard III, W. A. Dynamic transition in the structure of an energetic crystal during chemical reactions at shock front prior to detonation. *Phys. Rev. Lett.* **2007**, *99*, 148303.

(73) Bagri, A.; Mattevi, C.; Acik, M.; Chabal, Y. J.; Chhowalla, M.; Shenoy, V. B. Structural evolution during the reduction of chemically derived graphene oxide. *Nat. Chem.* **2010**, *2*, 581–587.

(74) LaBrosse, M. R.; Johnson, J. K.; Van Duin, A. C. T. Development of a transferable reactive force field for cobalt. *J. Phys. Chem. A* **2010**, *114*, 5855–5861.

(75) Ganesh, P.; Kent, P. R. C.; Mochalin, V. Formation, characterization, and dynamics

of onion-like carbon structures for electrical energy storage from nanodiamonds using reactive force fields. *J. Appl. Phys.* **2011**, *110*, 073506.

(76) Srinivasan, S. G.; van Duin, A. C. T. Molecular-Dynamics-Based Study of the Collisions of Hyperthermal Atomic Oxygen with Graphene Using the ReaxFF Reactive Force Field. *J. Phys. Chem. A* **2011**, *115*, 13269–13280.

(77) Huang, X.; Yang, H.; Van Duin, A. C. T.; Hsia, K. J.; Zhang, S. Chemomechanics control of tearing paths in graphene. *Phys. Rev. B* **2012**, *85*, 195453.

(78) Islam, M. M.; Ostadhossein, A.; Borodin, O.; Yeates, A. T.; Tipton, W. W.; Hennig, R. G.; Kumar, N.; van Duin, A. C. T. ReaxFF molecular dynamics simulations on lithiated sulfur cathode materials. *Phys. Chem. Chem. Phys.* **2015**, *17*, 3383–3393.

(79) Ostadhossein, A.; Cubuk, E. D.; Tritsaris, G. A.; Kaxiras, E.; Zhang, S.; van Duin, A. C. T. Stress effects on the initial lithiation of crystalline silicon nanowires: reactive molecular dynamics simulations using ReaxFF. *Phys. Chem. Chem. Phys.* **2015**, *17*, 3832–3840.

(80) Srinivasan, S. G.; van Duin, A. C. T.; Ganesh, P. Development of a ReaxFF potential for carbon condensed phases and its application to the thermal fragmentation of a large fullerene. *J. Phys. Chem. A* **2015**, *119*, 571–580.

(81) Verners, O.; van Duin, A. C. T. Comparative molecular dynamics study of fcc-Ni nanoplate stress corrosion in water. *Surf. Sci.* **2015**, *633*, 94–101.

(82) Wood, M. A.; Cherukara, M. J.; Kober, E. M.; Strachan, A. Ultrafast chemistry under nonequilibrium conditions and the shock to deflagration transition at the nanoscale. *J. Phys. Chem. C* **2015**, *119*, 22008–22015.

(83) Zou, C.; Shin, Y. K.; van Duin, A. C. T.; Fang, H.; Liu, Z.-K. Molecular dynamics simulations of the effects of vacancies on nickel self-diffusion, oxygen diffusion and

oxidation initiation in nickel, using the ReaxFF reactive force field. *Acta Mater.* **2015**, *83*, 102–112.

(84) Nielson, K. D.; Van Duin, A. C. T.; Oxgaard, J.; Deng, W.-Q.; Goddard, W. A. Development of the ReaxFF reactive force field for describing transition metal catalyzed reactions, with application to the initial stages of the catalytic formation of carbon nanotubes. *J. Phys. Chem. A* **2005**, *109*, 493–499.

(85) Goddard, W. A.; Van Duin, A.; Chenoweth, K.; Cheng, M.-J.; Pudar, S.; Oxgaard, J.; Merinov, B.; Jang, Y. H.; Persson, P. Development of the ReaxFF reactive force field for mechanistic studies of catalytic selective oxidation processes on BiMoO x. *Top. Catal.* **2006**, *38*, 93.

(86) Mueller, J. E.; Van Duin, A. C. T.; Goddard III, W. A. Development and validation of ReaxFF reactive force field for hydrocarbon chemistry catalyzed by nickel. *J. Phys. Chem. C* **2010**, *114*, 4939–4949.

(87) Zou, C.; Van Duin, A. Investigation of complex iron surface catalytic chemistry using the ReaxFF reactive force field method. *JOM* **2012**, *64*, 1426–1437.

(88) Shin, Y. K.; Kwak, H.; Vasenkov, A. V.; Sengupta, D.; van Duin, A. C. T. Development of a ReaxFF reactive force field for Fe/Cr/O/S and application to oxidation of butane over a pyrite-covered Cr2O3 catalyst. *ACS Catal.* **2015**, *5*, 7226–7236.

(89) Zhang, Q.; Çağın, T.; Van Duin, A.; Goddard III, W. A.; Qi, Y.; Hector Jr, L. G. Adhesion and nonwetting-wetting transition in the Al/α-Al$_2$O$_3$ interface. *Phys. Rev. B* **2004**, *69*, 045423.

(90) Chenoweth, K.; Cheung, S.; Van Duin, A. C. T.; Goddard, W. A.; Kober, E. M. Simulations on the thermal decomposition of a poly (dimethylsiloxane) polymer using the ReaxFF reactive force field. *J. Am. Chem. Soc.* **2005**, *127*, 7192–7202.

(91) Cheung, S.; Deng, W.-Q.; Van Duin, A. C. T.; Goddard, W. A. ReaxFF$_{MgH}$ reactive force field for magnesium hydride systems. *J. Phys. Chem. A* **2005**, *109*, 851–859.

(92) van Duin, A. C. T.; Zeiri, Y.; Dubnikova, F.; Kosloff, R.; Goddard III, W. A. Atomistic-scale simulations of the initial chemical events in the thermal initiation of triacetonetriperoxide. *J. Am. Chem. Soc.* **2005**, *127*, 11053–11062.

(93) Goddard III, W.; Merinov, B.; Van Duin, A.; Jacob, T.; Blanco, M.; Molinero, V.; Jang, S. S.; Jang, Y. H. Multi-paradigm multi-scale simulations for fuel cell catalysts and membranes. *Mol. Simulat.* **2006**, *32*, 251–268.

(94) Hong, S.; van Duin, A. C. T. Molecular dynamics simulations of the oxidation of aluminum nanoparticles using the ReaxFF reactive force field. *J. Phys. Chem. C* **2015**, *119*, 17876–17886.

(95) Verlackt, C.; Neyts, E.; Jacob, T.; Fantauzzi, D.; Golkaram, M.; Shin, Y. K.; van Duin, A. C. T.; Bogaerts, A. Atomic-scale insight into the interactions between hydroxyl radicals and DNA in solution using the ReaxFF reactive force field. *New J. Phys.* **2015**, *17*, 103005.

(96) Yeon, J.; van Duin, A. C. T. ReaxFF molecular dynamics simulations of hydroxylation kinetics for amorphous and nano-silica structure, and its relations with atomic strain energy. *J. Phys. Chem. C* **2015**, *120*, 305–317.

(97) Yue, D.-C.; Ma, T.-B.; Hu, Y.-Z.; Yeon, J.; van Duin, A. C. T.; Wang, H.; Luo, J. Tribochemical mechanism of amorphous silica asperities in aqueous environment: A Reactive Molecular Dynamics Study. *Langmuir* **2015**, *31*, 1429–1436.

(98) Mortier, W. J.; Ghosh, S. K.; Shankar, S. Electronegativity-equalization method for the calculation of atomic charges in molecules. *J. Am. Chem. Soc.* **1986**, *108*, 4315–4320.

(99) Rappe, A. K.; Goddard III, W. A. Charge equilibration for molecular dynamics simulations. *J. Phys. Chem.* **1991**, *95*, 3358–3363.

(100) Aktulga, H. M.; Fogarty, J. C.; Pandit, S. A.; Grama, A. Y. Parallel reactive molecular dynamics: Numerical methods and algorithmic techniques. *Parallel Comput.* **2012**, *38*, 245–259.

(101) Plimpton, S. Fast parallel algorithms for short-range molecular dynamics. *J. Comput. Phys.* **1995**, *117*, 1–19.

(102) Kylasa, S. B.; Aktulga, H. M.; Grama, A. Y. PuReMD-GPU: A reactive molecular dynamics simulation package for GPUs. *J. Comput. Phys.* **2014**, *272*, 343–359.

(103) Raghavachari, K.; Trucks, G. W.; Pople, J. A.; Head-Gordon, M. A fifth-order perturbation comparison of electron correlation theories. *Chem. Phys. Lett.* **1989**, *157*, 479 – 483.

(104) Dunning, T. H. Gaussian basis sets for use in correlated molecular calculations. I. The atoms boron through neon and hydrogen. *J. Chem. Phys.* **1989**, *90*, 1007–1023.

(105) Feyereisen, M.; Fitzgerald, G.; Komornicki, A. Use of approximate integrals in ab initio theory. An application in MP2 energy calculations. *Chem. Phys. Lett.* **1993**, *208*, 359 – 363.

(106) Bernholdt, D. E.; Harrison, R. J. Large-scale correlated electronic structure calculations: the RI-MP2 method on parallel computers. *Chem. Phys. Lett.* **1996**, *250*, 477 – 484.

(107) Halkier, A.; Helgaker, T.; Jørgensen, P.; Klopper, W.; Koch, H.; Olsen, J.; Wilson, A. K. Basis-set convergence in correlated calculations on Ne, N_2, and H_2O. *Chem. Phys. Lett.* **1998**, *286*, 243 – 252.

(108) Zhao, Y.; González-García, N.; Truhlar, D. G. Benchmark database of barrier heights for heavy atom transfer, nucleophilic substitution, association, and unimolecular reactions and its use to test theoretical methods. *J. Phys. Chem. A* **2005**, *109*, 2012–2018.

(109) Karton, A.; Sylvetsky, N.; Martin, J. M. L. W4-17: A diverse and high-confidence dataset of atomization energies for benchmarking high-level electronic structure methods. *J. Comput. Chem.* **2017**, *38*, 2063–2075.

(110) Yarkony, D. *Modern Electronic Structure Theory*; World Scientific: New Jersey, 1995; Vol. 2.

(111) Mardirossian, N.; Head-Gordon, M. ωB97M-V: A combinatorially optimized, range-separated hybrid, meta-GGA density functional with VV10 nonlocal correlation. *J. Chem. Phys.* **2016**, *144*, 214110.

(112) Mardirossian, N.; Head-Gordon, M. Thirty years of density functional theory in computational chemistry: an overview and extensive assessment of 200 density functionals. *Mol. Phys.* **2017**, *115*, 2315–2372.

(113) Behn, A.; Zimmerman, P. M.; Bell, A. T.; Head-Gordon, M. Efficient exploration of reaction paths via a freezing string method. *J. Chem. Phys.* **2011**, *135*, 224108.

(114) Baker, J. An algorithm for the location of transition states. *J. Comput. Chem.* **1986**, *7*, 385–395.

(115) Fukui, K. Formulation of the reaction coordinate. *J. Phys. Chem.* **1970**, *74*, 4161–4163.

(116) Ishida, K.; Morokuma, K.; Komornicki, A. The intrinsic reaction coordinate. An ab initio calculation for HNC $\longrightarrow$ HCN and H$^-$ + CH$_4$ $\longrightarrow$ CH$_4$ + H$^-$. *J. Chem. Phys* **1977**, *66*, 2153–2156.

(117) Schmidt, M. W.; Gordon, M. S.; Dupuis, M. The intrinsic reaction coordinate and the rotational barrier in silaethylene. *J. Am. Chem. Soc.* **1985**, *107*, 2585–2589.

(118) Shao, Y.; Gan, Z.; Epifanovsky, E.; Gilbert, A. T.; Wormit, M.; Kussmann, J.; Lange, A. W.; Behn, A.; Deng, J.; Feng, X., et al. Advances in molecular quantum chemistry contained in the Q-Chem 4 program package. *Mol. Phys.* **2015**, *113*, 184–215.

(119) Becke, A. D. Density-functional thermochemistry. III. The role of exact exchange. *J. Chem. Phys.* **1993**, *98*, 5648–5652.

(120) Lee, C.; Yang, W.; Parr, R. G. Development of the Colle-Salvetti correlation-energy formula into a functional of the electron density. *Phys. Rev. B* **1988**, *37*, 785.

(121) Krishnan, R.; Binkley, J. S.; Seeger, R.; Pople, J. A. Self-consistent molecular orbital methods. XX. A basis set for correlated wave functions. *J. Chem. Phys.* **1980**, *72*, 650–654.

(122) van Duin, A. C. T.; Baas, J. M. A.; Van De Graaf, B. Delft molecular mechanics: a new approach to hydrocarbon force fields. Inclusion of a geometry-dependent charge calculation. *J. Chem. Soc. Faraday Trans.* **1994**, *90*, 2881–2895.

(123) Pahari, P.; Chaturvedi, S. Determination of best-fit potential parameters for a reactive force field using a genetic algorithm. *J. Mol. Model.* **2012**, *18*, 1049–1061.

(124) Larsson, H. R.; Hartke, B. Fitting reactive force fields using genetic algorithms. *Comput. Method Mater. Sci.* **2013**, *13*.

(125) Larsson, H. R.; Van Duin, A. C. T.; Hartke, B. Global optimization of parameters in the reactive force field ReaxFF for SiOH. *J. Comput. Chem.* **2013**, *34*, 2178–2189.

(126) Shchygol, G.; Yakovlev, A.; Trnka, T.; van Duin, A. C. T.; Verstraelen, T. ReaxFF

Parameter Optimization with Monte-Carlo and Evolutionary Algorithms: Guidelines and Insights. *J. Chem. Theory Comput.* **2019**, *15*, 6799–6812.

(127) Nakata, H.; Bai, S. Development of a new parameter optimization scheme for a reactive force field based on a machine learning approach. *J. Comput. Chem.* **2019**, *40*, 2000–2012.

(128) Furman, D.; Wales, D. J. Transforming the Accuracy and Numerical Stability of ReaxFF Reactive Force Fields. *J. Phys. Chem. Lett.* **2019**, *10*, 7215–7223.

(129) Leven, I.; Head-Gordon, T. C-GeM: Coarse-Grained Electron Model for Predicting the Electrostatic Potential in Molecules. *J. Phys. Chem. Lett.* **2019**, *10*, 6820–6826.

Graphical TOC Entry